Magn Reson Mater Phy (2010) 23:217–226
DOI 10.1007/s10334-010-0219-6

RESEARCH ARTICLE

An oxygen-consuming phantom simulating perfused tissue to explore oxygen dynamics and ^{19}F MRI oximetry

Steven H(ubert) Baete · Jan Vandecasteele · Luc Colman · Wilfried De Neve · Yves De Deene

Received: 3 June 2009 / Revised: 31 May 2010 / Accepted: 1 June 2010 / Published online: 25 June 2010

Abstract
Objective This study presents a reproducible phantom which mimics oxygen-consuming tissue and can be used for the validation of ^{19}F MRI oximetry.
Materials and methods The phantom consists of a haemodialysis filter of which the outer compartment is filled with a gelatin matrix containing viable yeast cells. Perfluorocarbon emulsions can be added to the gelatin matrix to simulate sequestered perfluorocarbons. A blood-substituting perfluorocarbon fluid is pumped through the lumen of the fibres in the filter. ^{19}F relaxometry MRI is performed with a fast 2D Look-Locker imaging sequence on a clinical 3T scanner.
Results Acute and perfusion-related hypoxia were simulated and imaged spatially and temporally using the phantom.
Conclusions The presented experimental setup can be used to simulate oxygen consumption by somatic cells in vivo and for validating computational biophysical models of hypoxia, as measured with ^{19}F MRI oximetry.

Keywords Quantitative magnetic resonance imaging (qMRI) · ^{19}F MRI oximetry · Tumour hypoxia · Phantom · Fast T_1-imaging

S. H. Baete (✉) · J. Vandecasteele · W. De Neve · Y. De Deene
Department of Radiation Oncology and Experimental Cancer Research, Ghent University, De Pintelaan 185, 9000 Gent, Belgium
e-mail: steven.baete@ugent.be

S. H. Baete · Y. De Deene
MEDISIP-IBBT, Ghent University, De Pintelaan 185, 9000 Gent, Belgium

L. Colman
Faculty of Applied Engineering Sciences, University College Ghent, Schoonmeersstraat 52, 9000 Gent, Belgium

Introduction

Tumour hypoxia and necrosis result from an imbalance between oxygen (O_2) supply and consumption [1–4]. The decreased oxygen supply is caused mainly by the abnormal structure and function of the microvessels supplying the tumour cells and by the increased diffusion distances between nutritive blood capillaries and tumour cells. As a result, solid tumours are heterogeneous structures with significantly lower oxygen tensions (pO_2) than surrounding normal tissue [3]. Tumour hypoxia is well known to reduce cancer treatment efficacy [3], since hypoxic tumour cells are more resistant to both radiotherapy and chemotherapy. Chemotherapy is impaired by insufficient drug delivery [4] and higher resistance of hypoxic cells to some chemotherapeutic drugs. However, drugs selective for hypoxic cells are being researched [2]. Radiotherapy, on the other hand, is seen as less effective in tumour cell populations displaying pO_2 less than 10 mmHg in cervical cancer and less than 2.5 mmHg in head and neck cancer [5,4]; the indirect effect of oxygen radicals is an important contributor to the radiation damage. Additionally, hypoxic tumour cells experience changes in proteome and genome, enabling these cells to overcome nutritive deprivation or to escape their hostile environment [1].

The non-invasive diagnosis of tumour hypoxia could provide significant advances in cancer treatment. Recent studies have shown that MRI oximetry can be used as a predictor of tumour response to classical radiation therapy [6,7]. Moreover, combination of tumour hypoxia maps and biologically guided radiotherapy could improve therapy outcome [8]. Additionally, innovative image-guided conformal radiotherapy techniques enable targeting higher doses to hypoxic tumour regions (e.g. [9]), thus ensuring a better treatment.

Various methods for probing oxygen tensions pO_2 in tissue have been developed [2,4,10,11]. These methods include

polarographic microelectrodes [12–16], fibre optic fluorescence probes [17–19], near-infrared spectroscopy [14,20], nuclear hypoxia reporter probes [2,21] and various magnetic resonance imaging (MRI) techniques. Most of these methods, however, are highly invasive, have poor spatial resolution or fail to dynamically and quantitatively sample oxygen tensions [7]. Amongst available MRI techniques is blood oxygen level–dependent (BOLD) contrast. Although BOLD is considered to be sensitive to changes in blood oxygenation, it is also subject to contributions of additional physiological factors [4,11,22]. Another MRI technique exploits changes in tissue T_1 as a qualitative measure of pO_2 [23] in situations of oxygenation challenge (low- or high oxygen breathing). Recently, hexamethyldisiloxane, a ^{1}H MRI hypoxia probe, was shown to be able to quantitatively measure oxygen tension pO_2 [24]. This method, however, requires adequate water and fat suppression.

One of the more extensively studied MRI methods to detect tumour hypoxia is fluorine (^{19}F) MRI [4]. This technique uses perfluorocarbon (PFC) compounds as a marker for oxygenation; perfluorocarbons are hydrocarbons whose hydrogen atoms are exchanged for fluorine atoms. The transverse relaxation rate R_1 of these perfluorocarbons increases linearly with the dissolved oxygen concentration [25]. This proportionality can be used to sensitively and quantitatively measure interstitial oxygen concentrations. Moreover, research indicates that the R_1 of perfluorocarbons is independent of salt concentrations [26], pH [26,27], the presence of proteins [27] and emulsification [25].

In addition, perfluorocarbons exhibit high molecular oxygen solubility [11,25,28–31]. Consequently, the use of perfluorocarbons as blood substitutes for oxygen delivery has been studied extensively [32]. Furthermore, ^{19}F is 100% abundant (isotopically), the amount of endogenous fluorine in the body is very small and the endogenous fluorine exhibits very short T_2-relaxation times [11], resulting in the absence of a background signal. The gyromagnetic ratio γ of ^{19}F (40.05 MHz/T) is close to that of ^{1}H (42.58 MHz/T), and the relative sensitivity amounts to 83.2% relative to ^{1}H.

The potential of ^{19}F-oximetry has been demonstrated extensively, see [10,33] for a review of methods and perfluorocarbon compounds used. Oxygen tension measurements have been recorded in several animal models (e.g. rats [20,34–44], rabbits [45,46], mice [15,19,47] and pigs [48]) bearing several tumour models. The perfluorocarbon compounds are mainly administrated as emulsions, neat [37] or in alginate beads [44]. Emulsions are administered intravenously, while neat perfluorocarbons (hexafluorobenzene) are injected directly intra-tumoural (e.g. [10,37]), thus ensuring a high concentration of ^{19}F in the tumour itself. In contrast to emulsions and neat perfluorocarbons, alginate beads are sequestered for a long period at the implantation site, allowing for follow-up studies [44].

The distribution of perfluorocarbons, used as a marker for ^{19}F-oximetry, in the tumour tissue is dependent on the administration method [15,37,44]. Emulsified perfluorocarbons, injected intravenously, are sequestered close to blood vessels in well-perfused tumour areas [15]. As a result, measurements of pO_2 in badly perfused hypoxic regions may be underrepresented. This could bias the measurements towards the well perfused regions. Furthermore, these sequestered perfluorocarbon emulsions remain bound to structures in the tissue, rather than that they eventually redistribute in the tumour volume [15]. Neat perfluorocarbons on the other hand are mainly retained near the injection site. Although this allows sampling of pO_2 in badly perfused regions, it does not ensure a homogeneous distribution throughout the tumour volume [13,20,37,38]. Similarly, alginate beads are localised at the implantation site [44].

The validation of pO_2-measurement methods in vivo remains difficult. Previous validations compared ^{19}F-oximetry with polarographic probes [12–15], fibre optic fluorescence probes [18,19] and near-infrared spectroscopy [14,20]. Although these studies reported good correspondence with ^{19}F-oximetry, the in vivo comparisons suffered from the heterogeneity of animal tumour models. This tumour heterogeneity renders it difficult to compare point measurements such as those performed with fibre optic and polarographic probes with more global measurements such as near-infrared spectroscopy and ^{19}F-oximetry. Furthermore, the comparison of oximetry methods is hindered by the difference in quantities measured. While fibre optic, polarographic probes and ^{19}F-oximetry measure pO_2, near-infrared spectroscopy quantifies changes in oxygenated haemoglobin concentrations ($\Delta[HbO_2]$).

An objective method is needed for the quantitative comparison of the performance of new and existing imaging techniques and perfluorocarbons. Hence, in this study, a reproducible phantom, simulating well-perfused oxygen-consuming tissue, is presented. The phantom consists of a haemodialysis filter (Fig. 1). The hollow haemodialysis fibres represent blood vessels. The outer compartment of the filter, normally used for the dialysate fluid, simulates tissue. The tissue is represented by a gelatin matrix containing viable yeast cells (Saccharomyces cerevisiae). The yeast cells consume oxygen, when supplied, in a similar manner to tissue. On the other hand, in situations of oxygen deprivation, the yeast switches to anaerobic respiration. This increases the convenience of phantom handling as the phantom does not need to be respirated continuously. Yeast cells were used earlier [14,49] in a simpler setup to study the relationship between pO_2 and the change in oxygenated haemoglobin concentrations $\Delta[HbO_2]$ measured with a polarographic probe [14] and near-infrared spectroscopy [49]. In this setup, yeast cells caused a deoxygenation of a saline solution containing blood. Recent research has found no indication for negative

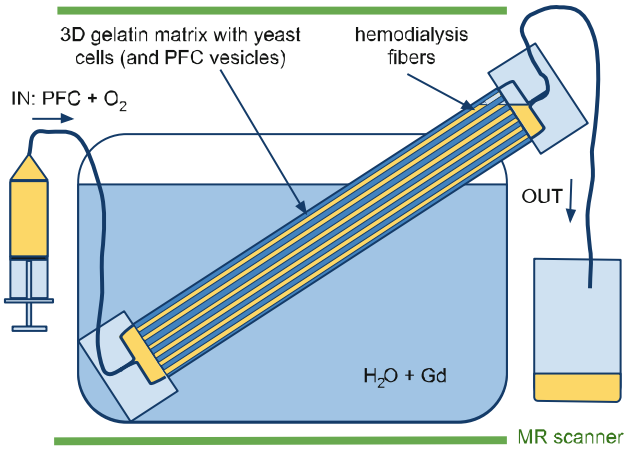

Fig. 1 Schematic of a phantom for the quantitative comparison of ^{19}F MRI-oximetry methods. The phantom consists of a haemodialysis filter placed in an MR-scanner and an automated syringe pump. The outer compartment of the filter is filled with a gelatin matrix containing viable yeast cells simulating oxygen-consuming tissue. Additionally, perfluorocarbon (PFC) vesicles can be added to the gelatin matrix to simulate sequestered PFC emulsions. A pump is used to circulate a blood-substituting fluid through the lumen of the fibres

influences of perfluorocarbons on the growth of yeast cells [50]. In other experiments, excised rat hearts, which were prelabelled with sequestered perfluorocarbon, were used to simulate the effects of ischaemia [38].

In the presented phantom, the flow of a blood-substituting fluid in the haemodialysis fibres is controlled by a homebuilt automated syringe pump. The fluid that is injected through the fibres could be a realistic blood substitute. When the blood substitute itself is well aerated, it also serves as an oxygen supply for the simulated tissue in the phantom. If perfluorocarbons or perfluorocarbon emulsions are added to the blood substitute, realistic in vivo imaging situations can be simulated. The blood-substituting perfluorocarbon fluid used for demonstration purposes in this study was hexafluorobenzene. The hexafluorobenzene supplies oxygen to the yeast cells in the system, thanks to its good oxygen solubility [30]. In addition, it serves as a marker for the oxygenation measurements. The flow of hexafluorobenzene through the haemodialysis filter is slow enough to ensure equilibrium of O_2 concentrations in and around the haemodialysis fibres. The flow speed of the blood-substituting fluid is slow compared to the measurement times, thus avoiding possible flow artefacts [51].

The applicability of a phantom to simulate living vascularised tissue is demonstrated in this study. The behaviour of the phantom is studied following an impulse flow of aerated hexafluorobenzene and during a constant in-flow of aerated hexafluorobenzene at different flow speeds. In an additional experiment, a perfluorocarbon emulsion is added to the gelatine matrix in order to simulate sequestered PFC. The reaction of the phantom in these situations is measured with ^{19}F MRI-oximetry.

Materials and methods

pO_2-measurements

^{19}F-MRI oximetry was performed with the perfluorocarbon hexafluorobenzene. Hexafluorobenzene (HFB; Fluorochem Old Glossop, Derbyshire, UK) exhibits a single ^{19}F resonance frequency. Furthermore, the spin-lattice relaxation rate R_1 of HFB shows exceptional sensitivity to changes in oxygen tension pO_2, whilst it is relatively insensitive to temperature changes [37]. The usage of hexafluorobenzene for in vivo oximetry has been demonstrated extensively (e.g. [7,10,19,37,41,47]). Besides hexafluorobenzene, other perfluorocarbon compounds and emulsions can be used in conjunction with the phantom.

The R_1-relaxation rate is measured using a fast 2D Look-Locker imaging sequence [19,52–55]. The usability of Look-Locker sequences for ^{19}F-oximetry mapping has recently been demonstrated [19]. In the sequence utilised in the present study (see Fig. 2), 32 read-out groups are recorded following an inversion pulse. Each read-out group probes the magnetisation at a different inversion time (TI). One read-out group comprises sixteen small flip angle (β) read-out pulses measuring different k-space lines. The k-space lines acquired in one read-out group contribute to one inversion time-weighted image. The resulting 32 inversion time-weighted images allow the calculation of R_1-maps. The duration of a read-out group needs to be small in comparison with the inversion time to avoid unequal T_1-weighting of k-space.

The fast 2D Look-Locker imaging sequence was implemented on a 3T scanner (Trio, Siemens, Erlangen, Germany). Both an in-house constructed single-tuned birdcage coil, with a diameter of 9.3 cm, and a commercially available double-tuned birdcage coil (^{19}F and ^{1}H, Rapid biomedical, Rimpar, Germany) were used for ^{19}F signal excitation and detection (resonance frequency 115.9 MHz). In the imaging sequence, a hyperbolic secant inversion pulse was found to give an optimal slice selection profile [53]. Imaging was performed with 400 ms between subsequent read-out groups ($TI_2 - TI_1$) and 10 ms between the sixteen read-out pulses in each read-out group. The other imaging parameters were repetition time (TR) 30 s, field-of-view (FOV) 100 mm, slice thickness 10 mm, matrix size (MS) 128 $\times$ 128, read-out pulse flip angle $\beta = 20°$. The in-plane resolution of the images was 0.78 mm. The total duration for acquiring one R_1 map was 4 min.

The R_1-maps were calculated offline by fitting an equation for the theoretical magnetisation [54] to the magnitude signals at different TI on a pixel-by-pixel basis.

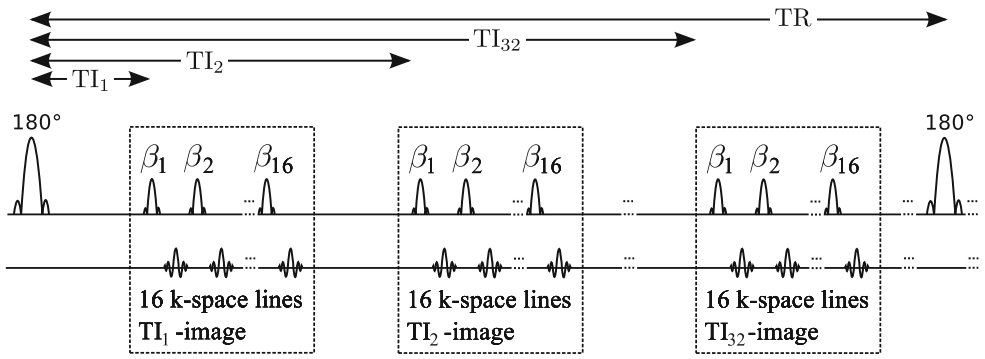

Fig. 2 Inversion recovery 2D Look-Locker imaging sequence. Each inversion pulse is followed by 32 read-out groups each containing sixteen read-outs with a small flip angle β. The *k*-space *lines* measured during one read-out group contribute to one image with a certain inversion time TI. The resulting 32 images, with $\mathrm{TI}_i (i = 1, \ldots, 32)$, are used to calculate R_1

For fitting, a non-linear least-squares method employing a Levenberg–Marquardt algorithm (Matlab, The Mathworks, USA) was used. The resulting R_1-maps were then used to calculate pO_2-maps using the calibrated relation $\mathrm{R}_1 = a = b\,\mathrm{pO}_2$.

Calibration of the pO_2-R_1 relation was performed with samples of pure hexafluorobenzene. The samples were deoxygenated by bubbling with N_2 (Air Liquide, Liège, Belgium) and then brought in equilibrium with gas mixtures ($\mathrm{O}_2/\mathrm{N}_2$) containing 0, 1.8, 5.7 and 21% O_2. Subsequently, the samples were sealed airtight in glass tubes, closed with blood-sampling tube stoppers (Terumo Europe, Leuven, Belgium). R_1 of the samples was measured with the same protocol as described above at 23°C. Finally, the equation $\mathrm{R}_1 = a + b\,\mathrm{pO}_2$ was fitted to the calibration data.

Phantom

The main component of the phantom is a haemodialysis filter (BLS819SD, Bellco S.p.a., Mirandola, Italy) [56] (Fig. 3). The cylindrical filter is filled with approximately 10^4 hollow haemodialysis fibres (DIAPES® HF800, Membrana GmbH, Wuppertal, Germany) directed along the axis of the cylinder. These tightly packed haemodialysis fibres, which are made of polyethersulfone, have an inner diameter of 200 µm, a wall thickness of 30 µm and an approximate pore size of 35 kDa. The hollow fibres mimic blood vessels in our model. The blood-substituting fluid is pumped through the inner compartment of the filter, through the lumen of the fibres. For this study, the luer lock connections of the inner compartment of the haemodialysis filter were adapted to accommodate ordinary flexible PVC tubing.

The tissue in the outer compartment of the haemodialysis filter is simulated by a hydrogel in which viable yeast cells are embedded. The gelatin gel is fabricated by dissolving gelatin (300 Bloom, type A, Sigma–Aldrich) [3%(w/w)] in tap water [38.05%(w/w)] at room temperature (approx. 23°C). Fresh yeast cells (Baker's yeast, ALGIST Bruggeman nv, Ghent, Belgium) [2%(w/w)] and glucose (Sigma–Aldrich) [0.4%(w/w)] are dispersed in tap water [54.55%(w/w)] at room temperature and left for 1 h. The glucose and the 1-h resting period allow the yeast to adjust to the new situation. Meanwhile, the gelatin solution is heated to 50°C in order to obtain a sol and left to cool down to 35°C. Methyleneblue solution (Sigma–Aldrich, 10 mg/ml solution in de-ionised water) [2%(w/w)] is added to the gelatin solution in order to visualise the yeast viability. Methyleneblue becomes colorless at low oxygen concentrations [57]. The yeast and the gelatin solution are then mixed gently and pumped in the outer compartment of the haemodialysis filter. The haemodialysis filter itself is preheated in a waterbath at approx 35°C to enhance hydrogel circulation. The hydrogel is pumped in a closed circuit until no more air bubbles emerge from the filter. After filling the inner compartment of the filter with N_2 (Air Liquide, Liège, Belgium), the phantom is left for 2–4 h. Finally, when the gel has solidified, the inner compartment is prefilled with (de-oxygenated) water or blood-substituting fluid in anticipation of the use of the phantom in an experiment.

In some experiments, sequestered PFC is simulated by replacing 10.05%(w/w) of the tap water in the gelatin solution with perfluorocarbon emulsion. For the perfluorocarbon emulsion, hexafluorobenzene [5%(w/w)], tap water [5%(w/w)] and sodiumdodecylsulphate (SDS, SigmaAldrich)) [0.05%(w/w)] are thoroughly mixed and pumped subsequently through several hypodermic needles of decreasing inner diameter (18G, 23G and $27\mathrm{G}^{1/2}$; Microlance™ 3, Becton Dickinson, Drogheda, Ireland). The perfluorocarbon emulsion is added to the yeast and gelatin solution mixture prior to filling the phantom. A 5%(w/w) concentration of hexafluorobenzene lies within the range of concentrations injected intravenously in in vivo animal experiments (e.g. [6,13,14,18,20]). When considering the dimensions of the phantom, the sequestered perfluorocarbons in the hydrogel

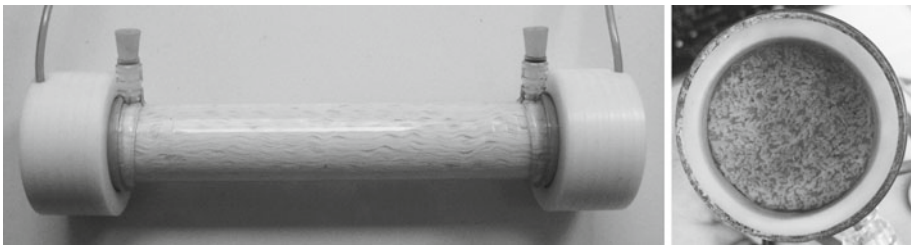

Fig. 3 (*Left*) Side view of haemodialysis filter with (altered) connections to the *inner* compartment at the sides of the filter and connections to the *outer* compartment, filled with hydrogel in this study, on the *top*. (*right*) Opened entrance part of the *inner* compartment of the haemodialysis filter showing the embedded hollow fibres

amount to 7.9% of the total perfluorocarbon content of the phantom.

The phantom is placed diagonally in the coil (Fig. 1) to avoid redirecting the flow of blood-simulating fluid to the bottom half of the filter. In addition, the phantom is surrounded by Gd-doped water to decrease susceptibility artefacts. The Gd-doped water is placed in the examination room (climatised at 23°C) 24 h before the start of the experiment. As a result, the water surrounding the phantom acts as a thermal buffer.

The flow of blood-simulating fluid in the phantom is controlled by a homebuilt syringe pump. For this purpose, a medical syringe (50 ml, Plastipak®, Becton Dickinson, Drogheda, Ireland) is mounted on a linear stage (PTW, Freiburg, Germany) using dedicated fittings. The linear stage can be operated with a small in-house-built software program. Alternatively, a volumetric pump (e.g. Alaris IVAC 590, Cardinal Health, Dublin, Ireland) can be used to control the flow. However, the flow control system in the latter type of pumps relies on a drop counter, and the low surface tension of hexafluorobenzene [58] prohibits adequate droplet formation in the drop counter.

Results

The relation $R_1 = a + b\,pO_2$ was calibrated with in vitro ^{19}F-MRI measurements of hexafluorobenzene samples for 4 different oxygen tensions at 23°C using a 3T clinical scanner. The calibration provided an intercept value of $a = 0.101 \pm 0.006 s^{-1}$ and a slope value of $b = 0.0231 \pm 0.0006\ s^{-1}\ \%\ atm^{-1}$. The slope of the pO_2-R_1 relation lies in between the values reported earlier at 7T [37] and 4.7T [19,39,41] and the values reported at 1.9T [47]. The relation $pO_2 = (R_1 - 0.101)/0.0231$, with pO_2 in %atm[1] and R_1 in s^{-1}, was used to calibrate our measurements.

The usage of the phantom simulating living vascularised tissue is demonstrated in two experimental situations. In the first experiment, the inner compartment of the phantom is prefilled with oxygen-rich hexafluorobenzene. In order to reach an oxygen-free initial situation, the yeast is allowed to consume the oxygen present in the filter. When the initial situation is reached, a bolus of oxygen-rich hexafluorobenzene is injected in the inner compartment of the filter. The reaction of the system to this impulse of oxygen supply is measured using ^{19}F-MRI oximetry. The time evolution of the oxygen tension pO_2 in a region of interest (roi, approx. 5 cm^3) in the phantom is plotted in Fig. 4. As the time post-bolus injection increases, the oxygen levels drop to zero.

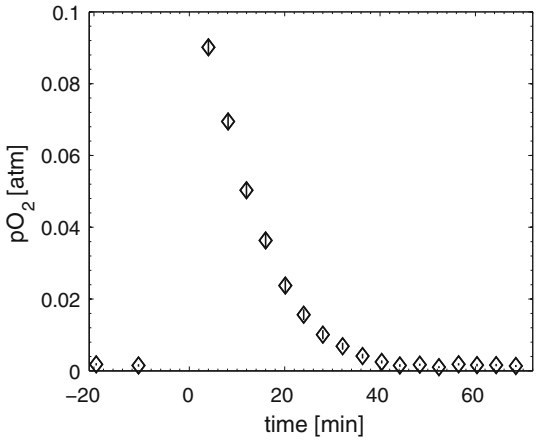

Fig. 4 Time evolution of oxygen tension pO_2 in a roi in the phantom following the injection of a bolus of oxygen-rich hexafluorobenzene in the *inner* compartment of the phantom (*inner* compartment of the haemodialysis filter, see Fig. 1). The *error bars* indicate the standard deviation of pO_2 in the roi

A second experiment simulates constant blood flow. Transverse pO_2-images (Fig. 5) illustrate the distribution of oxygen levels in the phantom at different times. Additionally, an experiment in which a perfluorocarbon emulsion is added to the outer compartment of the filter simulates the presence of sequestered perfluorocarbons in tissue. Hence, the influence of the sequestered perfluorocarbons on the pO_2-dynamics in the phantom was studied. Figure 6 shows both the evolution of oxygen tension pO_2 in a roi in the

[1] torr = mmHg = $\frac{760}{100}$ %atm.

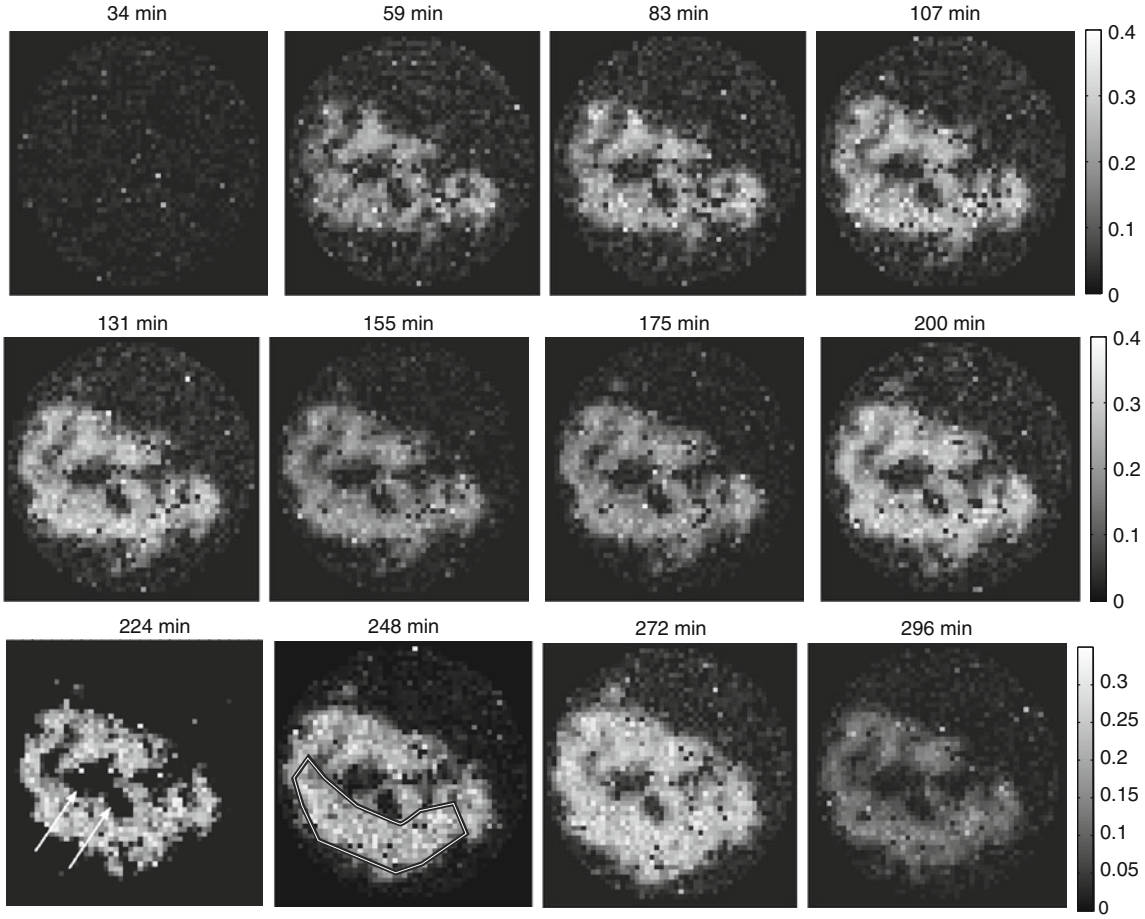

Fig. 5 Oxygen tension pO_2-images (pO_2 in atm) of a cross-section of the phantom, without perfluorocarbon emulsion in the hydrogel, at twelve subsequent times during the application of an in-flow of oxygen-rich hexafluorobenzene in the *inner* compartment of the phantom. The timing corresponds to the one shown in Fig. 6. The *arrows* indicate an area of decreased ^{19}F concentration. The roi indicated by a *solid line* is used for evaluation of the time evolution of pO_2 (plotted in Fig. 6) of the phantom not containing any perfluorocarbon emulsion in the hydrogel

phantom [with (square box) and without (diamond) perfluorocarbon emulsion, left axis] and the flow speed applied in the lumen of the fibres (–, right axis) (the timing in Fig. 6 corresponds with the timing in Fig. 5). After reaching an initial oxygen-free situation in a similar manner to the first experiment, a steady flow of oxygen-rich hexafluorobenzene is maintained through the inner compartment of the filter. The initial response of pO_2 to the flow of hexafluorobenzene in the phantom is delayed 15 min. This is the time needed for the oxygen-rich hexafluorobenzene to reach the location of the roi (approximately 5 cm distal of the flow entrance). For the smallest of the two flow speeds (from ±25 to ±210 min in Fig. 6), pO_2 continuously increases. At the end of this period of slow flow, pO_2 is almost saturated, suggesting a balance in oxygen supply and consumption. When the higher flow speed is applied (from ±210 to ±270 min in Fig. 6), pO_2 increases further to a higher concentration until an equilibrium in oxygen supply and consumption is reached. If perfluorocarbon emulsions are added to the outer compartment of the filter, the pO_2-levels increase faster at the beginning of the experiment and decrease at a slower pace when the flow is stopped. In the course of the flow scheme, the syringes in the syringe pump have to be refilled a few times. Although this procedure takes an experienced experimentator less than a minute, the dips in flow speed are clearly visible in the pO_2-curve.

The trend in pO_2-levels in the images (Fig. 5) of the second experiment is similar to the time evolution in the roi (Fig. 6). However, the distribution of pO_2 in this transverse slice of the filter shows inhomogeneities. The inhomogenous pO_2 distribution in the transverse direction of the filter is partially matched by the inhomogenous distribution of ^{19}F-signal in the same slice. An arrow in Fig. 7 (an ^{19}F-SE image of the same slice as in Fig. 5) indicates a region of decreased ^{19}F corresponding to areas of lower perfusion in the phantom (see arrows in Fig. 5). Additionally, the large area of low pO_2 in the top right of the transverse section of the slice in Fig. 5 arises from accumulation of yeast cells. These

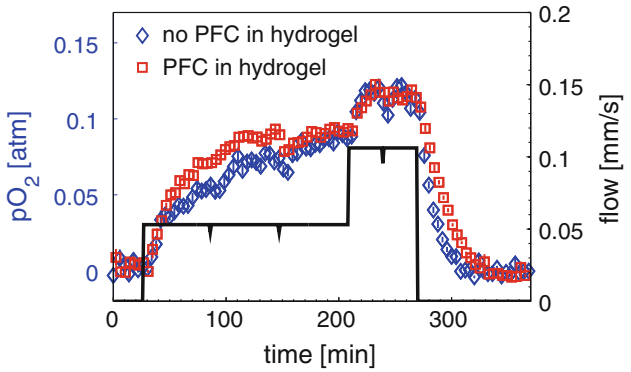

Fig. 6 Time evolution of oxygen tension pO_2 in a roi in the phantom [with (*square box*) and without (*diamond*) perfluorocarbon emulsion in the hydrogel, *left* axis] in reaction to the in-flow of oxygen rich hexafluorobenzene at different flow speeds (–, *right* axis) in the *inner* compartment of the phantom. The dips in flow speed mark the refilling of the syringe pump. The *error bars* indicate the standard deviation of pO_2 in the roi

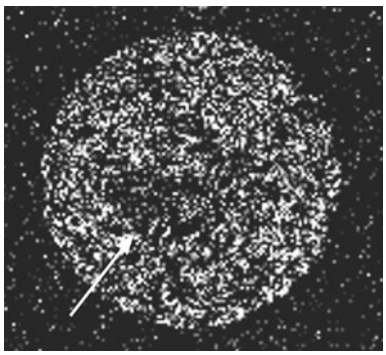

Fig. 7 Transverse ^{19}F-SE image of a cross-section of the phantom (slice identical to image 5), illustrating the distribution of hydrogel in the haemodialysis filter (repetition time (TR) 1760 ms, echo time (TE) 15 ms, field-of-view (FOV) 90 mm, slice thickness 10 mm). The *arrow* indicates an area of decreased ^{19}F concentration

yeast cells sank to the bottom during the gelation process when the filter was stored inverted (upside down relative to the position in Fig. 5). Larger concentrations of yeast cells indicate lower oxygen concentration as the oxygen consumption increases with yeast cell concentration. Furthermore, it was also found that the in-flow of oxygen in this slice is influenced by the yeast distribution in upstream parts of the haemodialysis filter. In any slice, both the oxygen content of the in-flowing hexafluorobenzene and the yeast distribution in the slice influence the pO_2-distribution.

Discussion

The results of the measurements performed with the presented phantom illustrate the feasibility of using this phantom setup as a model for living vascularised tissue. The yeast cells in the outer compartment of the filter emulate the oxygen consumption of living (tumour) tissue. This oxygen consumption allows the simulation and measurement of the distribution and evolution of oxygen levels in a controlled environment. Moreover, the oxygen consumption of the yeast allows simulation of pO_2-levels in an environment similar to living tissue. Additionally, oxygen tensions in the phantom can be studied both spatially (Fig. 5) and temporally (Figs. 4 and 6).

Hypoxia can originate in a number of mechanisms, most of which are perfusion-, diffusion- or anemia-related [1]. Perfusion-related (acute) hypoxia is caused by insufficient blood flow (e.g. fully or partially occluded blood vessels). The occlusion of an artery can be simulated in the phantom by abruptly stopping perfusion of the phantom (Fig. 6) or by studying the reaction of the phantom to a bolus of oxygen-rich blood-substituting fluid (Fig. 4). Low or insufficient oxygen supply (e.g. partially occluded vessels) can easily be simulated by limiting the in-flow of oxygen-rich blood-substituting fluid (Fig. 6) or by adjusting the oxygen content of the perfusion fluid. Perfusion-limited hypoxia can be seen in the phantom in Fig. 5 in the area just left beneath the center of the slice. In this area (pointed out by arrows in the images in Figs. 5 and 7), the concentration of ^{19}F is low indicating a bundle of occluded fibres. As a result, the in-flow of oxygen in this area is also lower, which can be described as perfusion-limited hypoxia. During the experiment, oxygen diffuses in from well-perfused areas nearby, and the size of the hypoxic area decreases. Anemia-related hypoxia, caused by a reduced O_2 transport capacity of blood, can be simulated in a similar manner as perfusion-related hypoxia by fine-tuning the oxygen content or the concentration of oxygen carriers in the perfusion fluid.

The simulation of diffusion-limited hypoxia is less controllable. Diffusion-limited hypoxia arises from increases in diffusion distances as the tumour expands. In the phantom, a phenomenon related to diffusion-limited hypoxia is present at the top right region of the slice in Fig. 5. This large area of low pO_2 arises from accumulation of yeast cells. During the gelation process of the hydrogel, the filter was stored inverted (upside down relative to the position in Fig. 5) and the yeast cells descended. Consequently, the concentration of fibres relative to the tissue (cell) density is low in that region. Although the unequal distribution of tissue density and fibres throughout the phantom could seem unwanted at first, it allows for the study of well and poorly vascularised regions in the phantom. The increased tissue to blood vessel ratio at the top right of the slice simulates, for instance, a poorly vascularised region. Unfortunately, it is difficult to control the formation of these areas for simulation purposes as they are inherent to the construction and the filling of the specific haemodialysis filter. However, minor changes in the preparation of the phantom hydrogel, such as acclimatising

the haemodialysis filter to be filled in a waterbath and faster subsequent cooling, allow for a more homogeneous distribution of yeast throughout the phantom volume. On the other hand, it is possible to selectively occlude a number of hollow fibres (Fig. 3) and induce diffusion-related hypoxia in a more controlled manner.

The presence of sequestered perfluorocarbons in tissue is simulated by dispersing a perfluorocarbon emulsion in the hydrogel in the outer compartment of the phantom. The experiment with constant flow of oxygen-rich hexafluorobenzene in the fibres of the phantom, as shown in Fig. 6, was performed with and without sequestered perfluorocarbons. The results of these experiments reveal two notable differences when perfluorocarbon emulsions are added to the hydrogel. A first difference arises at the start of oxygen in-flow. At that time, starting from an initial oxygen-free situation, the pO_2-levels increase faster if perfluorocarbons are present in the hydrogel. This is attributed to the increased absorption of oxygen (carried by the passing hexafluorobenzene) by the hydrogel because of the higher oxygen solubility of the hydrogel–perfluorocarbon emulsion mixture. Due to the high oxygen solubility, the sequestered perfluorocarbons act as oxygen reservoirs. However, pO_2 saturates to an approximately identical level in both experiments when oxygen consumption and supply balance (after $\pm$175 min in Fig. 6). When saturated, the pO_2 in the sequestered perfluorocarbons is in equilibrium with the pO_2 of the surrounding hydrogel. Consequently, the oxygen dissolved in the sequestered perfluorocarbons delays changes of pO_2-level in the surrounding hydrogel. This pO_2-level is determined by the balance between oxygen consumption and supply in the hydrogel. The second difference appears when oxygen in-flow stops. The yeast needs more time to consume the additional oxygen present in the sequestered perfluorocarbons and pO_2 decreases at a slower rate in the gel containing sequestered perfluorocarbons than in the hydrogel without any perfluorocarbons.

Figure 6 shows that sequestered perfluorocarbons artificially increase the oxygen concentrations in the hydrogel. Note that the data in Fig. 6 are expressed as oxygen pressures. The sequestered perfluorocarbons will increase the oxygen solubility of the hydrogel, thus increasing dissolved oxygen concentrations at equal oxygen pressure. These observations indicate that sequestered perfluorocarbons may alter the oxygen concentrations in the tumour tissue. As a result, the measured actual oxygen concentrations in tissue may be higher than the originial oxygen concentrations before administration of perfluorocarbons. Moreover, this arises even when the sequestered perfluorocarbons are homogeneously dispersed in the tissue, as demonstrated here. The increased oxygen concentration, caused by the presence of sequestered perfluorocarbons could, however, possibly help increase the radiation sensitivity of hypoxic tissues. Further studies of the influence of sequestered perfluorocarbons on the tissue oxygen concentration could remove the perfluorocarbons from the blood-substituting fluid or use different perfluorocarbons for sequestration and blood-substituting fluid [59]. These setups would allow a detailed study of the influence of sequestered perfluorocarbons on oxygen concentrations in tissue.

The oxygen-consuming capacity of the hydrogel arises from the viable yeast cells in the gelatin matrix. Baker's yeast cells are easily obtainable and require little attention. The yeast cells can survive relatively long periods of oxygen deprivation, which increases the convenience of phantom handling. As a result, baker's yeast cells are the ideal unicellular microorganisms for this application. For the simulation of specific tissues or experimental setups, other microorganisms could also be used. The concentration of (yeast) cells can be altered, if necessary, to adjust the oxygen-consuming capacity of the simulated tissue.

The phantom's main component is a haemodialysis filter. It is easily available, in larger quantities if necessary, and it provides a simple model of vascularised tissue. As a lot of haemodialysis filters are commercially available, the specific properties of the filter (e.g. materials, porosity and packing of the hollow fibres) can be chosen to agree with experimental demands (e.g. [56,60]). The simple setup of parallel fibres in the haemodialysis filter allows for reproducible evaluation of oximetry techniques. Although computer simulations have shown that the heterogeneous structure of tumour microvasculature increases the occurrence of hypoxia (e.g. [61]) when compared to homogeneously structured microvasculature, a heterogeneous structure is not required for oximetry technique evaluation. In addition, a disadvantage of possible heterogeneous phantoms is the difficulty to reproduce them. A minor practical problem with the haemodialysis filters, in our experience, is the mechanically weak luer lock connections of the inner compartment. In the course of experiments presented in this study, the connections had to be replaced by stronger in-house fabricated polyoxymethylene connections.

The usage of the phantom is demonstrated in this study with hexafluorobenzene as blood-substituting fluid. The hexafluorobenzene acts both as oxygen carrier and as marker for ^{19}F-MRI oximetry. In more advanced studies, a realistic blood-substituting fluid could be used. Moreover, several perfluorocarbons and perfluorocarbon emulsions could be compared quantitatively in the same phantom. In addition, nutrients for the embedded microorganisms can be added to the blood-substituting fluid.

The results in this study show that the presented phantom can be used for quantitative validation and comparison of MRI oximetry techniques. Additionally, the phantom's simple parallel fibre setup makes it easily reproducible. The potential of hypoxia markers and imaging sequences can be quantitatively assessed.

Conclusions

A phantom designed to simulate living vascularised tissue is presented. The fibres in the haemodialysis filter represent blood vessels, while the addition of viable yeast cells to a gelatin gel permits the simulation of oxygen-consuming tissue. Perfluorocarbon emulsions, added to the hydrogel, simulate sequestered perfluorocarbons. The evolution of oxygen tension pO_2 in the phantom is shown, illustrating the oxygen consumption by the yeast cells in the phantom after injection of a bolus of hexafluorobenzene and during a constant flow of oxygen. The phantom can be used to simulate oxygen consumption by somatic cells in vivo, for simulating several hypoxia situations and for validating ^{19}F-MRI oximetry.

Acknowledgments This research is supported by grants # 01J13507 and # 01D21208 from the BOF-Ghent University. S. Baete is a PhD Fellow of the Research Foundation—Flanders (FWO). The authors would like to thank students Cedric Aelterman and Robbe Coolsaet (University College Ghent) for the construction of a ^{19}F birdcage coil; and master student Nadia Van Geel for assistance in optimising the hydrogel composition. The authors are also thankful to Bart Truyens, Sam De Poorter and Robert De Greef for the adaptation of the haemodialysis filters and the fabrication of the syringe fittings, to Sunny Eloot for providing haemodialysis filters and to Eric Billiet for placing a volumetric pump at our disposal. Furthermore, the authors would like to thank two anonymous reviewers for their valuable remarks.

References

1. Vaupel P, Harrison L (2004) Tumor hypoxia: causative factors, compensatory mechanisms, and cellular response. Oncologist 9(S5):4–9
2. Tatum J, Kelloff G, Gillies R, Arbeit J, Brown J, Chao K, Chapman J, Eckelman W, Fyles A, Giaccia A, Hill R, Koch C, Krishna M, Krohn K, Lewis J, Mason R, Melillo G, Padhani A, Powis G, Rajendran J, Reba R, Robinson S, Semenza G, Swartz H, Vaupel P, Yang D, Croft B, Hoffman J, Liu G, Stone H, Sullivan D (2006) Hypoxia: Importance in tumor biology, noninvasive measurement by imaging, and value of its measurement in the management of cancer therapy. Int J Radiat Biol 82(10):699–757
3. Verma A (2006) Oxygen-sensing in tumors. Curr Opin Clin Nutr Metab Care 9(4):366–378
4. Davda S, Bezabeh T (2006) Advances in methods for assessing tumor hypoxia in vivo: implications for treatment planning. Cancer Metastasis Rev 25(3):469–480
5. Overgaard J, Horsman MR (1996) Modification of hypoxia-induced radioresistance in tumors by the use of oxygen and sensitizers. Semin Radiat Oncol 6(1):10–21
6. Zhao D, Constantinescu A, Chang C-H, Hahn E, Mason R (2003) Correlation of tumor oxygen dynamics with radiation response of the dunning prostate R3327-HI tumor. Radiat Res 159:621–631
7. Bourke VA, Zhao D, Gilio J, Chang CH, Jiang L, Hahn EW, Mason RP (2007) Correlation of radiation response with tumor oxygenation in the dunning prostate R3327-AT1 tumor. Int J Radiat Oncol Biol Phys 67(4):1179–1186
8. Stewart R, Li A (2007) BGRT: biologically guided radiation therapy—the future is fast approaching!. Med Phys 34(10):3739–3751
9. Vanderstraeten B, Duthoy W, Gersem WD, Neve WD, Thierens H (2006) [18F]fluoro-deoxy-glucose positron emission tomography ([18F]FDG-PET) voxel intensity-based intensity-modulated radiation therapy (IMRT) for head and neck cancer. Radiother Oncol 79(3):249–258
10. Zhao D, Jiang L, Mason RP (2004) Measuring changes in tumor oxygenation. Meth Enzymol 386:378–418
11. Kodibagkar VD, Wang X, Mason RP (2008) Physical principles of quantitative nuclear magnetic resonance oximetry. Front Biosci 13:1371–1384
12. Mason R, Shukla H, Antich P (1993) In vivo oxygen tension and temperature: simultaneous determination using 19F NMR spectroscopy of perfluorocarbon. Magn Reson Med 29:296–302
13. Zhao D, Constantinescu A, Hahn E, Mason R (2002) Differential oxygen dynamics in two diverse dunning prostate R3327 rat tumor sublines (MAT-Lu and HI) with respect to growth and respiratory challenge. Int J Radiat Oncol Biol Phys 53(3):744–756
14. Kim J, Zhao D, Song Y, Constantinescu A, Mason R, Liu H (2003) Interplay of tumor vascular oxygenation and tumor pO2 observed using near-infrared spectroscopy, an oxygen needle electrode, and 19F MR pO2 mapping. J Biomed Opt 8(1):53–62
15. van der Sanden B, Heerschap A, Simonetti A, Rijken P, Peters H, Stüben G, van der Kogel A (1999) Characterization and validation of noninvasive oxygen tension measurements in human glioma xenografts by 19F-MR relaxometry. Int J Radiat Oncol Biol Phys 44(3):649–658
16. Doll CM, Milosevic M, Pintilie M, Hill RP Fyles AW (2003) Estimating hypoxic status in human tumors: a simulation using Eppendorf oxygen probe data in cervical cancer patients. Int J Radiat Oncol Biol Phys 55(5):1239–1246
17. Griffiths JR, Robinson SP (1999) The OxyLite: a fibre-optic oxygen sensor. Br J Radiol 72(859):627–630
18. Zhao D, Constantinescu A, Hahn E, Mason R (2001) Tumor oxygen dynamics with respect to growth and respiratory challange: investigation of the dunning prostate R3327-HI tumor. Radiat Res 156:510–520
19. Jordan B, Cron G, Gallez B (2009) Rapid monitoring of oxygenation by 19F magnetic resonance imaging: simultaneous comparison with fluorescence quenching. Magn Reson Med 61:634–638
20. Xia M, Kodibagkar V, Liu H, Mason RP (2006) Tumour oxygen dynamics measured simultaneously by near-infrared spectroscopy and 19F magnetic resonance imaging in rats. Phys Med Biol 51:45–60
21. Krohn KA, Link JM, Mason RP (2008) Molecular imaging of hypoxia. J Nucl Med 49:129–148
22. Baudelet C, Gallez B (2002) How does blood oxygen level-dependent (BOLD) contrast correlate with oxygen partial pressure (pO2) inside tumors? Magn Reson Med 48(6):980–986
23. Matsumoto K-I, Bernardo M, Subramanian S, Choyke P, Mitchell J, Krishna MC, Lizak M (2006) MR assessment of changes of tumor in response to hyperbaric oxygen treatment. Magn Reson Med 56(2):240–246
24. Kodibagkar V, Cui W, Merritt M, Mason R (2006) Novel 1H NMR approach to quantitative tissue oximetry using hexamethyldisiloxane. Magn Reson Med 55(4):743–748
25. Parhami P, Fung BM (1983) Fluorine-19 relaxation study of perfluorochemicals as oxygen carriers. J Phys Chem 87(11):1928–1931
26. Thomas SR, Pratt RG, Millard RW, Samaratunga RC, Shiferaw Y, Clark LC, Hoffmann RE (1994) Evaluation of the influence of the aqueous phase bioconstituent environment on the F-19 T1 of perfluorocarbon blood substitute emulsions. J Magn Reson Imaging 4(4):631–635

27. Eidelberg D, Johnson G, Barnes D, Tofts PS, Delpy D, Plummer D, McDonald W (1988) 19F NMR imaging of blood oxygenation in the brain. Magn Reson Med 6(3):344–352
28. Delpuech J-J, Hamza M, Serratrice G, Stébé M-J (1979) Fluorocarbons as oxygen carriers. I. An NMR study of oxygen solutions in hexafluorobenzene. J Chem Phys 70(6):2680–2687
29. Hamza M, Serratrice G, Stébé M-J, Delpuech J-J (1981) Solute-solvent interactions in perfluorocarbon solutions of oxygen. An NMR study. J Am Chem Soc 103:3733–3738
30. Battino R, Rettich T, Tominaga T (1983) The solubility of oxygen and ozone in liquids. J Phys Chem Ref Data 12(2):163–178
31. Costa MF, Gomes JD, Menz D-H (2004) Solubility of dioxygen in seven fluorinated liquids. J Fluor Chem 125(9):1325–1329
32. Winslow RM (2005) Blood substitutes. 1. Academic Press, New York
33. Yu J-X, Kodibagkar V, Cui W, Mason R (2005) 19F: a versatile reporter for non-invasive physiology and pharmacology using magnetic resonance. Curr Med Chem 12(7):819–848
34. Fishman JE, Joseph PM, Carvlin MJ, Saadi-Elmandjra M, Mukherji B, Sloviter HA (1989) In vivo measurements of vascular oxygen tension in tumors using MRI of a fluorinated blood substitute. Invest Radiol 24(1):65–71
35. Dardzinski B, Sotak C (1994) Rapid tissue oxygen tension mapping using 19F inversion-recovery echo-planar imaging of Perfluoro-15-crown-5-ether. Magn Reson Med 32(1):88–97
36. Shukla H, Mason R, Woessner D, Antich P (1995) A comparison of three commercial perfluorocarbon emulsions as high-field 19F NMR probes of oxygen tension and temperature. J Magn Reson B 106(2):131–141
37. Mason R, Rodbumrung W, Antich P (1996) Hexafluorobenzene: a sensitive 19F NMR indicator of tumor oxygenation. NMR in Biomed 9(3):125–134
38. Shukla H, Mason R, Bansal N, Antich P (1996) Regional myocardial oxygen tension: 19F MRI of sequestered perfluorocarbon. Magn Reson Med 35:827–833
39. Le D, Mason R, Hunjan S, Constantinescu A, Barker B, Antich P (1997) Regional tumor oxygen dynamics: 19F PBSR EPI of hexafluorobenzene. Magn Reson Med 15(8):971–981
40. Hunjan S, Mason R, Constantinescu A, Peschke P, Hahn E, Antich P (1998) Regional tumor oximetry: 19F NMR spectroscopy of hexafluorobenzene. Int J Radiat Oncol Biol Phys 41(1):161–171
41. Hunjan S, Zhao D, Constantinescu A, Hahn EW, Antich PP, Mason RP (2001) Tumor oximetry: demonstration of an enhanced dynamic mapping procedure using fluorine-19 echo planar magnetic resonance imaging in the Dunning prostate R3327-AT1 rat tumor. Int J Radiat Oncol Biol Phys 49(4):1097–1108
42. Zhao D, Constantinescu A, Jiang L, Hahn EW, Mason RP (2001) Prognostic radiology: quantitative assessment of tumor oxygen dynamics by MRI. Am J Clin Oncol 24(5):462–466
43. Fan X, River J, Zamora M, Al-Hallaq H, Karczmar G (2002) Effect of carbogen on tumor oxygenation: combined fluorine-19 and proton MRI measurements. Int J Radiat Oncol Biol Phys 54(4):1202–1209
44. Nöth U, Rodrigues L, Robinson S, Jork A, Zimmermann U, Newell B, Griffiths J (2004) In vivo determination of tumor oxygenation during growth and in response to carbogen breathing using 15C5-loaded alginate capsules as fluorine-19 magnetic resonance imaging oxygen sensors. Int J Radiat Oncol Biol Phys 60(3):909–919
45. Lee H, Price RR, Holburn GE, Partain CL, Adams MD, Cacheris WP (1994) In vivo fluorine-19 MR imaging: relaxation enhancement with Gd-DTPA. J Magn Reson Imaging 4(4):609–613
46. Guo Q, Mattrey R, Guclu C, Buxton R, Nalcioglu O (1994) Monitoring of pO2 by spin-spin relaxation rate 1/T2 of 19F in a rabit abscess model. Art Cells Blood Subs Immob Biotech 22(4):1449–1454
47. McIntyre DJO, McCoy CL, Griffiths JR (1999) Tumour oxygenation measurements by F-19 magnetic resonance imaging of perfluorocarbons. Curr Sci 76(6):753–762
48. Thomas SR, Pratt RG, Millard RW, Samaratunga RC, Shiferaw Y, Mcgoron AJ, Kim KT (1996) In vivo pO_2 imaging in the porcine model with perfluoro carbon F-19 NMR at low field. Magn Reson Imaging 14(1):103–114
49. Liu H, Gu Y, Kim J, Mason R (2004) Near-infrared spectroscopy and imaging of tumor vascular oxygenation. Method Enzymol 386:349–378
50. Pilarek M, Szewczyk K (2008) Effects of perfluorinated oxygen carrier application in yeast, fungi and plant cell suspension cultures. Biochem Eng J 41(1):38–42
51. Higuchi T, Naruse S, Horikawa Y, Hirakawa K, Tanaka C (1988) In vivo measurement of the partial pressure of oxygen in brain tissue using 19F-NMR. Proc 7th Soc Magn Res Med 1:435
52. Brix G, Schad L, Deimling M, Lorenz W (1990) Fast and precise T1 imaging using a TOMROP sequence. Magn Reson Imaging 8(4):351–356
53. Gowland PA, Leach MO (1992) Fast and accurate measurements of T1 using a multi-readout single inversion-recovery sequence. Magn Reson Med 26(1):79–88
54. Nkongchu K, Santyr G (2005) An improved 3-D Look-Locker imaging method for T1 parameter estimation. Magn Reson Imaging 23(7):801–807
55. Nkongchu K, Santyr G (2007) Phase-encoding strategies for optimal spatial resolution and T1 accuracy in 3D Look-Locker imaging. Magn Reson Imaging 25(8):1203–1214
56. Ronco C, Ballestri M, Brendolan A (2000) New developments in hemodialyzers. Blood Purif 18(4):267–275
57. Sumitani M, Takagi S, Tanamura Y, Inoue H (2004) Oxygen indicator composed of an organic/inorganic hybrid compound of methylene blue, reductant, surfactant and saponite. Anal Sci 20(8):1153–1157
58. Freire M, Carvalho P, Queimada A, Marrucho I, Coutinho J (2006) Surface Tension of liquid fluorocompounds. J Chem Eng Data 51(5):1820–1824
59. Partlow KC, Chen JJ, Brant JA, Neubauer AM, Meyerrose TE, Creer MH, Nolta JA, Caruthers SD, Lanza GM, Wickline SA (2007) F-19 magnetic resonance imaging for stem/progenitor cell tracking with multiple unique perfluorocarbon nanobeacons. FASEB J 21:1647–1654
60. Deppisch R, Storr M, Buck R, Gohl H (1998) Blood material interactions at the surfaces of membranes in medical applications. Sep Purif Technol 14:241–254
61. Secomb T, Hsu R, Braun R, Ross J, Gross J, Dewhirst M (1988) Theoretical simulation of oxygen transport to tumors by three-dimensional networks of microvessels. Adv Exp Med Biol 454:629–634